Check for updates

Advanced Optical Materials

ADVANCED OPTICAL MATERIALS
www.advopticalmat.de

RESEARCH ARTICLE

Boosting Single-Molecule Fluorescence Enhancement With Nanoaperture-Nanoantenna Hybrid Systems

Ting Chen[1] | Zheyuan Zhu[1] | Boyi Liu[1] | Qiong He[2] | Lei Zhou[2] | Yan-Wen Tan[1]

[1]State Key Laboratory of Surface Physics and Department of Physics, Shanghai Key Laboratory of Metasurfaces for Light Manipulation, Multiscale Research Institute of Complex Systems, Nano Photonic Structures (Ministry of Education), Fudan University, Shanghai, China | [2]State Key Laboratory of Surface Physics and Department of Physics, Shanghai Key Laboratory of Metasurfaces for Light Manipulation, Nano Photonic Structures (Ministry of Education), Fudan University, Shanghai, China

Correspondence: Qiong He (qionghe@fudan.edu.cn) | Lei Zhou (phzhou@fudan.edu.cn) | Yan-Wen Tan (ywtan@fudan.edu.cn)

Received: 3 May 2026 | **Revised:** 13 October 2026 | **Accepted:** 26 October 2026

Keywords: electron beam lithography | fluorescence enhancement | nanoantennas | nanophotonics | plasmonics | single-molecule detection

ABSTRACT

Boosting the sensitivity of single-molecule fluorescence detection (SMFD), an unique tool in bio- and medical sciences, can be enabled by optical nanoantennas exhibiting hotspots to enhance light-matter interactions. However, precisely delivering molecules into hotspots with nanoscale sizes remains a great challenge for conventional nanoantennas with open interfaces. Here, we integrate carefully designed PMMA-substrated titanium nanoapertures with nanoantennas, and experimentally demonstrate that the hybrid systems can enhance the signal-to-background ratio of SMFD by up to 16 times compared to bare nanoantennas, although requiring higher molecular concentrations to achieve comparable detection efficiency. We design and fabricate a series of hybrid systems, and experimentally show that the unique "nanoaperture-confined hotspot" configuration formed in our systems can significantly enhance the probability of molecules accessing the hotspot region and shield low-enhancement events outside the hotspot region, thereby enhancing the single-molecular fluorescence signals with narrower enhancement distributions and diminished background signals. Our strategy can find many applications in bio- and medical sciences, such as single-molecule sequencing, surface-enhanced optical sensing, and so on.

1 | Introduction

Single-molecule fluorescence detection (SMFD) can probe the dynamic processes one molecule at a time, providing detailed information on molecular conformation and interaction kinetics, which offers unique understanding of functional mechanisms in biological systems [1, 2]. However, fluorescence signal emitted by a single molecule is extremely weak compared to overall background, making the signal-to-background ratio (SBR) poor and severely constraining the temporal and spatial resolution of SMFD [3].

Optical nanoantennas (e.g., noble-metal nanorods and nanoparticle dimers) [4–6], exhibiting tailored electromagnetic hotspots with strongly enhanced local fields [7–9], were widely used to manipulate the molecular excitation and quantum yield for molecular emission [10–12], thereby enhancing molecular fluorescence and suppressing photobleaching [13, 14]. These unique properties suggest that optical nanoantennas can help achieve ultrasensitive molecular detection at the single-molecule level [15–17], significantly broadening the applicability of SMFD [18, 19]. However, in a conventional nanoantenna with an open interface, the hotspot is confined to cover a limited region,

Ting Chen and Zheyuan Zhu contributed equally to this work.

All rights reserved, including rights for text and data mining and training of artificial intelligence technologies or similar technologies.
© 2026 Wiley-VCH GmbH

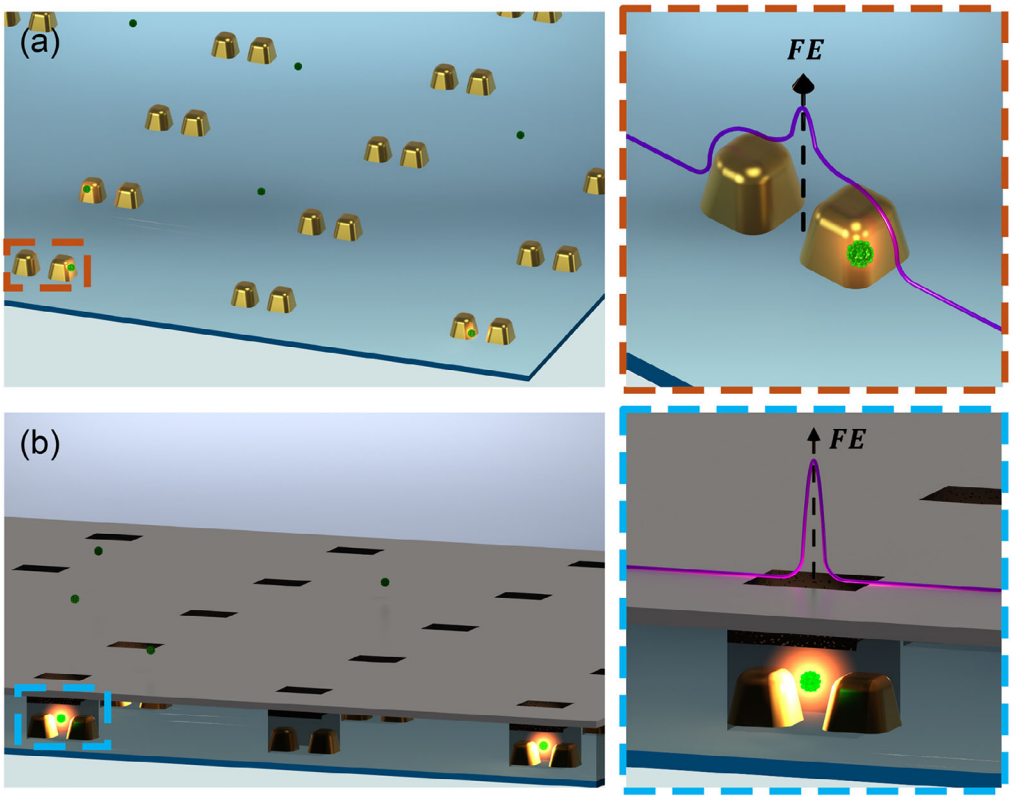

FIGURE 1 | Scheme of conventional nano-system with bare nanoantenna array (a) and our novel architecture combining plasmonic nanoantennas with nanoapertures (b) for florescence enhancement. Right panels of (a) and (b) illustrate individual nanostructures with fluorescence enhancement profiles (purple lines) for conventional bare nanoantennas (extending substantially beyond the hotspot boundary) and for our hybrid nano-system (primarily concentrated within the hotspot region). Molecules are represented as green, grape-like spheres. Their fluorescence signal is weak in (a) (depicted by faint yellow glow), due to the open interface of bare nanoantennas which severely limits molecular access to the tiny hotspot region. Conversely, the signal is strong in (b) (depicted by intense yellow glow), as the hybrid system utilizes nanoaperture mask to shield the non-hotspot regions of the nanoantennas, substantially increasing the probability of molecules entering the hotspot.

whereas the areas exhibiting fluorescence enhancement substantially extend beyond the hotspot boundary (see Figure 1a). Such an *undecorated* fluorescence enhancement distribution makes a bar nanoantenna exhibit a low SBR for SMFD, since 1) molecules are extremely difficult to access the tiny hotspot region, and 2) while increasing the overall molecular concentration can raise the number of molecules accessing the hotspots [20, 21], it also generates a substantial background signal since more molecules can scatter into the non-hotspot region with non-zero enhancements.

On the other hand, nanoapertures possess the intrinsic ability to confine the detection volume, allowing only molecules that enter the nanoapertures to be detected, thereby enabling background-free optical detection [22]. Consequently, they have been widely employed in DNA sequencing [23, 24], protein conformational dynamics [25, 26], single-molecule trapping [27, 28], and nanopore sensing [29–31]. However, conventional nanoapertures provide only weak electromagnetic field enhancements [32–34], which severely limits the fluorescence enhancement from molecule-nanoaperture interactions. Although efforts have been recently devoted to combine nanoapertures with nanoantennas forming an "antenna-in-a-box" platform [35–37], the adopted nanoaperture exhibits a size much larger than the hotspot, thus only providing a limited enhancement on SMFD performance.

Here, we propose a novel architecture integrating optical nanoantennas with optimized nanoaperture openings (see Figure 1b), and experimentally demonstrate that the hybrid system significantly enhances SMFD performance over conventional nanoantennas, achieving up to 16 times enhancement on SBR. We show that the nanoapertures can selectively shield the non-hotspot regions of nanoantennas while exposing the hotspots to target molecules, thereby significantly increasing their probabilities of accessing the hotspots. Concurrently, the nanoapertures reshape the fluorescence enhancement distributions by amplifying the occurrence of high-enhancement events within the hotspots while effectively suppressing low-enhancement events outside the aperture regions. These combined effects enable this unique configuration to further enhance the fluorescence signals and suppress the background noises. We design and fabricate a series of nanoaperture–nanoantenna hybrid systems, and experimentally demonstrate that they can achieve average fluorescence enhancements 4.4–6.3 times higher than their bare nanoantenna counterparts, with proper nanoantenna gap size and an asymmetric design exhibiting better performances. We further demonstrate experimentally that the nanoaperture size must be optimized to maximize fluorescence enhancement, as it balances two competing effects—nanoaperture entry probability and hotspot excitation probability. Compared to existing "antenna-in-a-box" strategies, our approach not only achieves the predicted maximum fluorescence enhancement with a narrower

21951071, 2026, 42, Downloaded from https://advanced.onlinelibrary.wiley.com/doi/10.1002/adom.72016 by Fudan University, Wiley Online Library on [15/11/2026]. See the Terms and Conditions (https://onlinelibrary.wiley.com/terms-and-conditions) on Wiley Online Library for rules of use; OA articles are governed by the applicable Creative Commons License

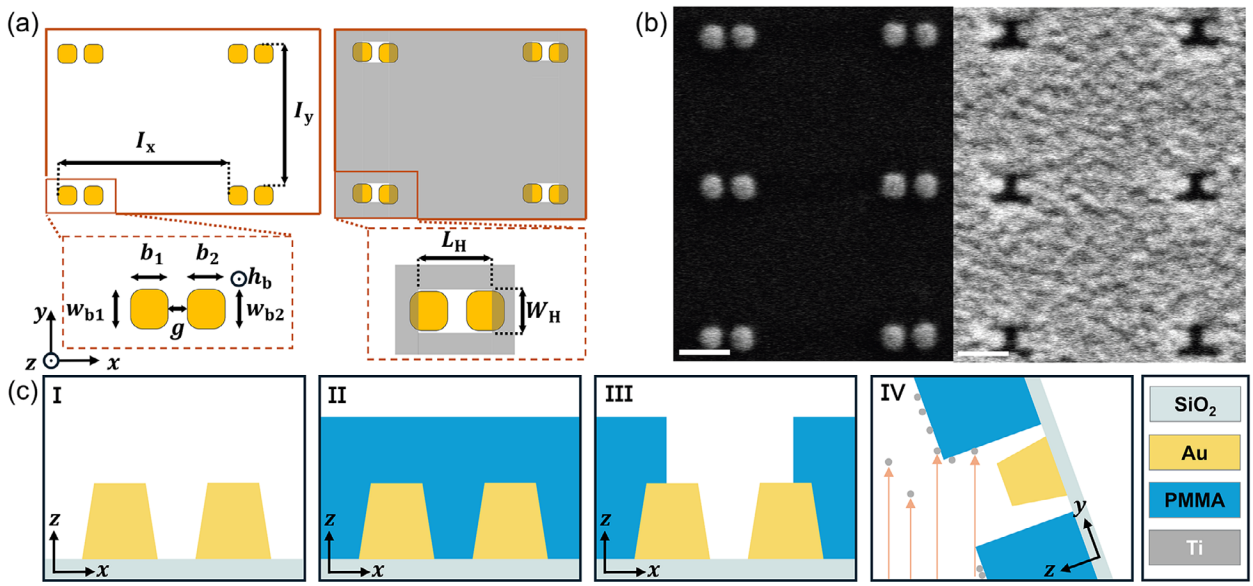

FIGURE 2 | Design and fabrication of our nanoaperture-nanoantenna hybrid system. (a) and (b) Schematics and scanning electron microscopy images of the nanoantenna-only system (left) and the hybrid system (right), respectively. Scale bar: 100 nm. The geometric parameters in (a) are defined as: nanoantenna bar lengths b_1, b_2; bar widths w_{b1}, w_{b2}; bar height h_b; gap size g; X-direction spacing I_x; Y-direction spacing I_y. Ti nanoaperture length L_H; width W_H. (c) Fabrication process of the hybrid system. Note that the planar coordinate system shown in Step IV differs from that in Steps I-III. The thicknesses of PMMA and Ti layer for our hybrid nano-systems are 75 and 10 nm, respectively.

distribution but also offers superior performance in low-concentration detection.

2 | Results and Discussion

2.1 | Realization of Hybrid Systems and Our Experimental Setup

Figure 2a depicts the schematic geometries of a typical double-bar nanoantenna (left) and the hybrid system (right) consisting of a nanoantenna array covered by a PMMA nanoaperture mask with a titanium (Ti) coating. The rectangular nanoapertures are precisely aligned with the nanoantenna gaps (i.e., hotspot regions). Fabrications of such optical systems involve sequential processing of preformed nanoantenna arrays (Step I), followed by resist-spinning (Step II), electron-beam lithography (Step III), and oblique-angle electron-beam evaporation of Ti layer (Step IV), as illustrated in Figure 2c (see Sample Preparation Section for more details). Figure 2b contains scanning electron microscopy pictures of a typical hybrid system (right panel) and the corresponding bare nanoantenna array (left panel). We use gold (Au) as the plasmonic metal to fabricate our nanoantennas, with resonant peaks tuned to the 500–600 nm excitation/emission band of visible dyes (see Figures S1–S4 and Tables S1 and S2 in Section S1). This selection represents a deliberate compromise informed by the following considerations. While silver offers superior optical properties [38], its rapid oxidation and challenging fabrication are incompatible with our multi-step process. Aluminum, though suitable for shorter wavelengths, exhibits significant losses in the green spectrum, limiting enhancement performance [34, 39]. Ti was selected primarily as the cladding materials for its superior resistance to biofouling and their reliability in biosensing applications, as after systematical experimental evaluation (see Figure S5 in Section S2). We note that the top Ti aperture layer is purposely designed to not in metallic contact with the bottom nanoantenna layer, which is essential to preserve the original resonances of our nanoantennas without adding more metallic losses. Achieving this required precise matching between the oblique evaporation angle during deposition, the Ti nanoaperture width, and the Ti layer thickness. As illustrated in Step IV of Figure 2c, depositing Ti obliquely causes metal accumulation on the aperture walls, significantly reducing the effective nanoaperture width. To ensure the nanoapertures remained open while maintaining an effective separation between the Ti edges and the underlying nanoantenna, we selected an oblique evaporation angle of 70°, a Ti aperture width of 50 nm, and a Ti layer thickness of 10 nm. Another critical trade-off involves the PMMA thickness, excessively thick PMMA creates high-aspect-ratio apertures that block dye diffusion into the hotspot, while insufficient PMMA risks Ti–Au contact during oblique deposition (see Figure S6). A thickness of 75 nm was chosen to balance molecular accessibility and structural integrity. We also investigated the influence of the nanoaperture shielding both experimentally and numerically, and found that its effect on the resonance peak position was quite weak (see Figure S4).

We fabricate a series of hybrid systems and their bare-antenna counterparts with different geometrical parameters, and experimentally characterize their fluorescence enhancement performances. Primary characterization was performed using a home-built total internal reflection (TIRF) wide-field microscope as shown in Figure 3a under low dye concentration conditions. In these experiments, the nano-systems are immersed in dye-containing solution at tens of nanomolar (nM) concentration and are excited by a 532 nm laser (see Fluorescence Experimental Setup Section for more details). This low concentration requirement is constrained by the thickness of the Ti masking

21951071, 2026, 42, Downloaded from https://advanced.onlinelibrary.wiley.com/doi/10.1002/adom.72016 by Fudan University, Wiley Online Library on [15/11/2026]. See the Terms and Conditions (https://onlinelibrary.wiley.com/terms-and-conditions) on Wiley Online Library for rules of use; OA articles are governed by the applicable Creative Commons License

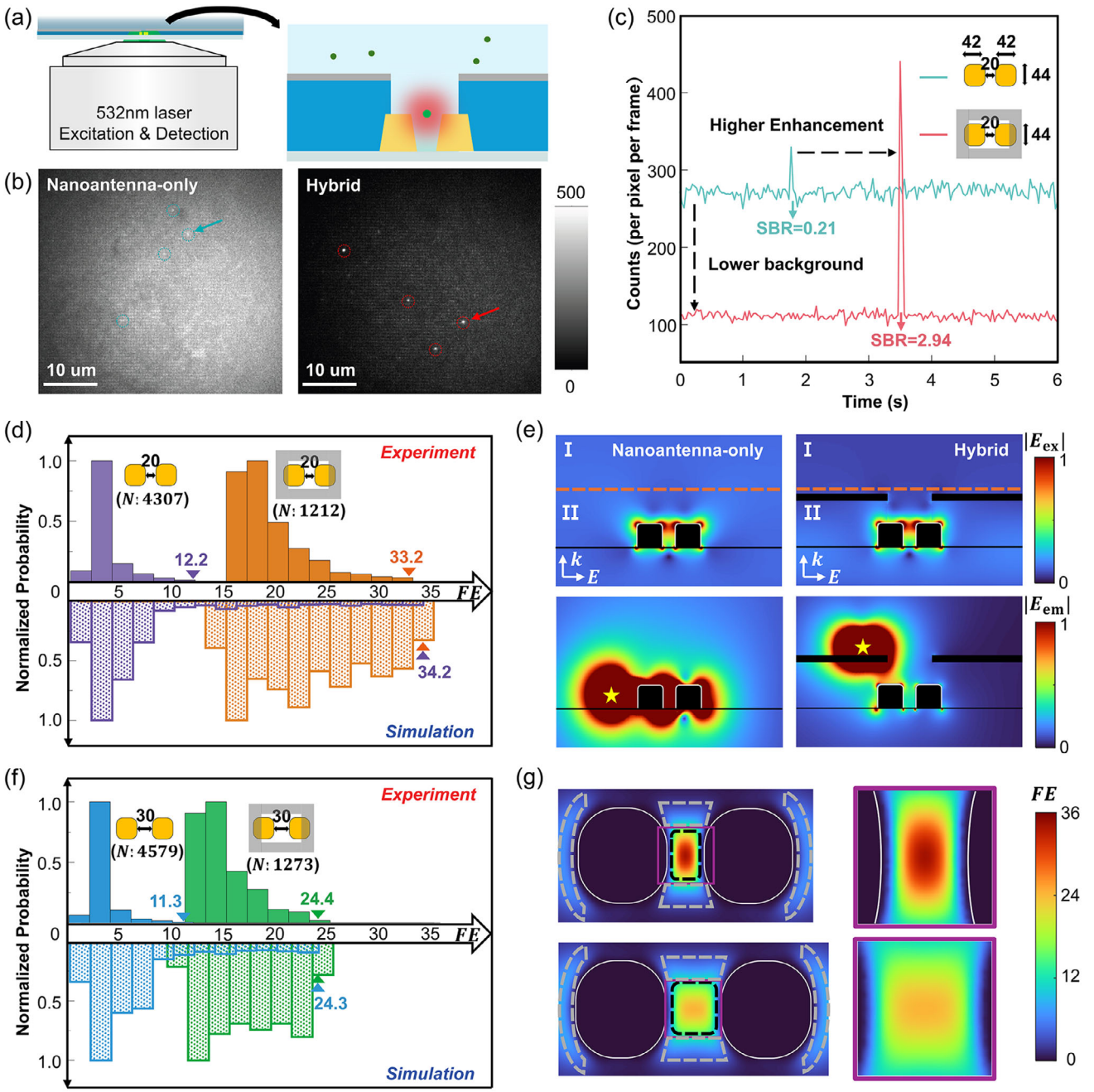

FIGURE 3 | Fluorescence enhancement of Alexa555 by various nano-systems. (a) Fluorescence experimental setup via inverted total internal reflection fluorescence (TIRF) microscope. (b) Fluorescence images of the nanoantenna-only system (left) and the nanoaperture-nanoantenna hybrid system (right) with $g = 20$ nm, respectively. Acquired using a unified intensity scale. Bright fluorescence spots marked by cyan (left) and red (right) circles. (c) Fluorescence intensity versus time traces (cyan: nanoantenna-only system; red: hybrid system) from arrow-marked regions in (b). (d) Fluorescence enhancement distributions of various nano-systems with $g = 20$ nm. Purple/orange: nanoantenna-only/hybrid systems. Fill/dot: experimental/simulated distributions. (e) Simulated field distributions for excitation (top) and emission (bottom) processes in the nanoantenna-only system (left) and the hybrid system (right). The excitation field is divided by orange dashed lines into Region I (solution zone) and Region II (below Ti layer). Yellow asterisks: fluorescent molecules. Black solid lines: glass substrate-nanoantenna interface. Simulation planes normal to the substrate. The axes labels $\boldsymbol{k}$ and $\boldsymbol{E}$ denote the wave vector (propagation direction) and electric field vector (polarization direction) of the excitation field, respectively. (f) Fluorescence enhancement distributions of various nano-systems with $g = 30$ nm. Blue/green: nanoantenna-only/hybrid systems. Fill/dot: experimental/simulated distributions. (g) Simulated fluorescence enhancement distributions on the plane of maximum enhancement (parallel to the substrate) for the double bar nanoantenna. Top/bottom: nanoantennas with $g = 20/30$ nm. Left: full structure (purple-outlined gap); right: gap magnified. Gray dashed boxes: non-hotspot regions; black dashed boxes: hotspot regions. In (d) and (f), fluorescence enhancement distributions within (hotspot + non-hotspot)/hotspot regions in (g) are assigned to the nanoantenna-only/hybrid systems' simulated distributions, N is the number of detected molecules and the FE_{max}s are marked with arrows and text of the corresponding color. Nanoantenna parameters: $b_1 = b_2 = 42$ nm; $w_{b1} = w_{b2} = 44$ nm; $h_b = 40$ nm; $g = 20$ or 30 nm; $I_x = 360$ nm; $I_y = 300$ nm. Nanoaperture parameters: $L_H = 80$ nm, $W_H = 50$ nm.

21951071, 2026, 42, Downloaded from https://advanced.onlinelibrary.wiley.com/doi/10.1002/adom.72016 by Fudan University, Wiley Online Library on [15/11/2026]. See the Terms and Conditions (https://onlinelibrary.wiley.com/terms-and-conditions) on Wiley Online Library for rules of use; OA articles are governed by the applicable Creative Commons License

layer (~10 nm), which is dictated by the nanoaperture opening dimensions and the oblique evaporation angle required during fabrication (see Figure 2c and Sample Preparation Section). At this thickness, Ti masking layer can reduce the fluorescence background from the dye-containing solution by approximately 61% (see Figure S7b,c in Section S3), enabling optimal SBR at lower dye concentrations. However, such low concentrations inherently limit the molecular detection throughput of our hybrid systems (see Table S3). To compensate for this limitation while maintaining statistical significance, we employed TIRF microscopy to simultaneously capture fluorescence signals from hundreds of nanoantennas across a wide field of view, ensuring sufficient molecule counts for robust statistical analysis without compromising the SBR-optimized detection conditions. This approach also underscores the enhanced capability of our hybrid systems for trace detection. Additionally, we employed fluorescence correlation spectroscopy (FCS) using a home-built confocal microscope to test the fluorescence enhancement performance of four representative nano-systems under high dye concentration conditions (10 μM). In these high-concentration experiments, also excited by the 532 nm laser (see Fluorescence Experimental Setup Section), we measured FCS trajectories with laser polarization both parallel and perpendicular to the nanoantenna long axis. The FCS analysis corroborates the fluorescence enhancement results obtained under the low-concentration conditions.

We estimate the fluorescence enhancement factor (FE) from the ratio of fluorescence intensity (after subtraction of fluorescence background) with and without the nano-systems (i.e., the nanoantennas or the hybrid systems):

$$FE = \frac{I_n}{I_g} \tag{1}$$

here, I_n and I_g represent the single-molecule fluorescence intensities obtained from the experimental groups (with nano-system) and the glass-only reference groups (without nano-system), respectively. These intensities are obtained directly by detecting fluorescence bursts generated when individual molecules traverse the focal volume. For the low-concentration TIRF experiments, due to the time resolution limitations of the camera (33 ms), we need to identify whether the detected fluorescence bursts originate from monomeric single molecules. Therefore, we first perform FCS experiments on the sample solution to verify the monomeric state of dyes in solution (see Figure S8 and Tables S4 and S5 in Section S4). Using the derived single-molecule diffusion times, we establish a TIRF data screening protocol (see Figures S9 and S10) to effectively exclude signals from molecular clusters. Comprehensive methodological details are provided in the TIRF Data Screening Methods Section and Section S4. The fluorescence enhancement distribution for each experimental group is determined by recording the intensities of all screened molecules, which are normalized against the average intensity of the corresponding glass reference group (see Figure S7a,b). For the high-concentration FCS experiments, the average fluorescence enhancement factor, molecular number, and diffusion time are derived directly by fitting the measured auto-correlation function curves. Comprehensive methodological details for the high-concentration FCS analysis and fluorescence enhancement extraction are provided in Section S5.

2.2 | Fluorescence Enhancement by a Typical Hybrid System

Taking a typical hybrid system with inter-bar distance g = 20 nm as an example, we experimentally characterize the fluorescence enhancement enabled by such a hybrid system compared with its bare-antenna counterpart, using a common yellow-greenish organic dye Alexa555. All other geometrical parameters of these two nano-systems are the same and specified in the caption of Figure 3. Figure 3b compares typical fluorescence images recorded for the nanoantenna-only system (left) and our hybrid system (right), under the experimental conditions with 10 nM concentration of Alexa555 and observation time of 90 s. Our hybrid system demonstrates significantly stronger single-molecule signals (red-circled spots) and reduced background noises (including scattering background from the nano-system, see Table S6 in Section S5) as compared to the nanoantenna-only system (cyan-circled spots), leading to a substantial improvement on SBR. This finding is further corroborated in Figure 3c, where the SBR of fluorescence intensity-time trajectories from a representative single molecule in the hybrid system (indicated by red arrow in Figure 3b) exhibits a 14 times enhancement over its counterpart in the nanoantenna-only system (indicated by cyan arrow in Figure 3b).

Statistical analyses of the measured fluorescence enhancement distribution for two different nano-systems (top panel in Figure 3d) further reveal their distinct enhancement capabilities. First of all, we note that our hybrid system can achieve a maximum fluorescence enhancement factor (FE_{max}) which is 2.73 times higher than that of the nanoantenna-only system. However, FE_{max} represents the enhancement experienced by only a small fraction of molecules. To comprehensively compare the fluorescence enhancement capabilities of two nano-systems, we calculate the arithmetic mean of enhancement values across all N molecules within each system, defined as the average fluorescence enhancement factor (FE_{avg}):

$$FE_{avg} = \frac{\sum_{i=1}^{i=N} FE_i}{N} \tag{2}$$

Comparison shows that the hybrid system exhibits an FE_{avg} that is 5.46 times higher than that of the nanoantenna-only system. This increase exceeds the gain in FE_{max}, indicating the enhanced uniformity of the fluorescence enhancement experienced by individual dye molecules within the hybrid system. To quantitatively characterize this uniformity, we define the relative width of the fluorescence enhancement distribution as:

$$W_{rel} = (FE_{max} - FE_{min}) \; / \; FE_{avg} \tag{3}$$

where FE_{min} is the minimum fluorescence enhancement factor achieved in each system. A smaller W_{rel} indicates a narrower distribution and thus a higher uniformity of the enhancement among molecules. Calculations based on experimentally measured data show that the hybrid system achieves a 69% decrease in W_{rel} compared to its nanoantenna-only counterpart (see Figure S11). Furthermore, incorporating the gain in FE_{avg} and the reduction in fluorescence background, we can calculate

21951071, 2026, 42, Downloaded from https://advanced.onlinelibrary.wiley.com/doi/10.1002/adom.72016 by Fudan University, Wiley Online Library on [15/11/2026]. See the Terms and Conditions (https://onlinelibrary.wiley.com/terms-and-conditions) on Wiley Online Library for rules of use; OA articles are governed by the applicable Creative Commons License

the average SBR gain ($\bar{G}_{SBR}$) achieved by the hybrid system as [37]:

$$\bar{G}_{SBR} = \frac{\overline{SBR}_{hyb}}{\overline{SBR}_{ao}} = \frac{FE_{avg,hyb}}{FE_{avg,ao}} \times \frac{Bg_{ao}}{Bg_{hyb}} \quad (4)$$

here, $\overline{SBR}_{hyb}$ and $\overline{SBR}_{ao}$ denote the average SBR of the hybrid system and the nanoantenna-only system, respectively, $FE_{avg,hyb}$ and $FE_{avg,ao}$ represent their corresponding average fluorescence enhancement, and Bg_{hyb} and Bg_{ao} indicate their respective fluorescence background intensities (shown in Figure 3c). Based on this equation, we find that the hybrid system achieves a 13.3 times improvement in average SBR, a gain that fully outweighs the associated reduction in molecular detection efficiency to 27.8% of the nanoantenna-only system (see Table S3).

Furthermore, under high-concentration conditions (10 μM Alexa555), the hybrid system demonstrates significantly superior fluorescence enhancement performance compared to the nanoantenna-only system (see Figures S12–S14 and Tables S7 and S8). The hybrid system achieves an FE_{avg} of 83.7 times, which is 6.44 times greater than that of the nanoantenna-only control (FE_{avg} = 13). Concurrently, the hybrid system achieves 63% fluorescence background suppression, increasing the average SBR by 17.8 times compared to the nanoantenna-only counterpart, surpassing even our low-concentration results. This conclusively demonstrates the comprehensive performance advantage of the hybrid system in micromolar-range high-concentration environments.

After accounting for the nanostructure's effect on single-molecule diffusion times, the high-concentration FCS results provide strong corroboration for the low-concentration TIRF measurements. Due to the limited time resolution (33 ms) of the TIRF camera, the *FE* measured by TIRF reflects the enhancement in the total photons emitted per diffusion event, rather than the instantaneous intensity enhancement at the microsecond scale, which is instead probed by FCS measurements. Consequently, alterations in single-molecule diffusion times induced by the nanostructures directly impact the *FE* obtained via TIRF. The confocal control group (no nanostructures) measured a diffusion time $\tau_{D,0}$ = 57.2 μs for Alexa555 molecules. For the hybrid system and its corresponding nanoantenna-only counterpart, the diffusion times of the enhanced molecules $\tau_{D,FE}$ shortened to 12.7 μs and 16.9 μs, respectively. Based on the correlation between diffusion time and the enhancement in total photons per diffusion event, we relate the FE_{avg} measured by high-concentration FCS to that measured by low-concentration TIRF using the following expression:

$$FE_{norm} = FE_{avg} \times \tau_{D,FE} / \tau_{D,0} \quad (5)$$

The FE_{norm} calculated from the FCS results are 18.5 times for the hybrid system and 3.9 times for the nanoantenna-only system. These values show excellent agreement with the TIRF-measured values of 19.4 times for the hybrid system and 3.6 times for the nanoantenna-only system, respectively (see the error analysis in Figures S15 and S16). Additionally, the FCS fitting reveals that the number of enhanced molecules ($N_{FE} \approx 1$) in the hybrid system is significantly lower than in the conventional nanoantenna system ($N_{FE} \approx 1.5$). This observation is consistent with the reduced molecular capture observed for the hybrid system in the TIRF measurements.

We perform numerical simulations on two nano-systems to elucidate the underlying physics. Figure 3e presents the simulated field distribution for excitation (top-panel) and radiation (bottom-panel) process by utilizing the finite element method (FEM) (see more simulation details in Section S6), illustrating how the nanoaperture mask enhances the SBR. As shown in region I of the top panel in Figure 3e, the Ti layer effectively blocks electromagnetic waves from below, thereby significantly reducing the field intensity in the solution above the metallic layer compared to the nanoantenna-only system. In the radiation process (bottom panel of Figure 3e), the Ti layer also prevents molecules outside the nanoaperture from strongly coupling with the nanoantenna. Collectively, these two effects markedly suppress the background fluorescence signals in the hybrid system. Furthermore, the nanoaperture mask in the hybrid system confines molecules primarily within the nanoantenna hotspot region, further significantly increasing the probability of detecting high-enhancement events during our experiments, by restricting most low-enhancement events. Consequently, under experimental conditions with low dye concentration and short observation time, where the spatial restriction reduces the total number of detectable molecules, the hybrid system exhibits a higher measured FE_{avg} and remarkably uniform fluorescence enhancement in the statistical analysis. In sharp contrast, dye molecules in the nanoantenna-only system can reside anywhere within the excitation region (Figure 3e bottom left panel). While such a broad spatial distribution enables detection of larger molecule counts, most molecules fail to occupy the hotspot region under identical conditions, resulting in substantially lower measured FE_{max} and FE_{avg} values compared to the hybrid system, accompanied by highly scattered enhancement factors. Notably, to reduce computational complexity, we simplified the nanoaperture component within the hybrid system model by replacing its realistic 3D Ti nanostructure with a 2D equivalent-thickness nanoaperture construct (see Figures S17 and S18). This simplification accurately reproduced the essential optical characteristics of the realistic structure. Furthermore, field distributions in two systems (hybrid and nanoantenna-only) only exhibit minor differences in the excitation process (Figure 3e top panel region II and Figure S19), indicating that the resonant mode is nearly independent of the Ti layer — a sharp departure from conventional "antenna-in-a-box" designs that significantly attenuate excitation fields (see Figure S20) [35]. This distinct advantage underscores the uniqueness of our hybrid architecture. Critically, the resonant mode's independence from the Ti layer enables a computational simplification: in our subsequent analyses, we minimize computational demands by estimating the hybrid system's *FE* from its nanoantenna-only counterpart's distribution rather than calculating it directly.

We quantitatively analyze the measured fluorescence enhancement distributions of two nano-systems from FEM simulations, by calculating the enhancement distributions on the plane exhibiting a maximum enhancement (parallel to the substrate) for the double bar nanoantenna with g = 20 nm (Figure 3g top panel). The total *FE* enabled by a nano-system is calculated

21951071, 2026, 42, Downloaded from https://advanced.onlinelibrary.wiley.com/doi/10.1002/adom.72016 by Fudan University, Wiley Online Library on [15/11/2026]. See the Terms and Conditions (https://onlinelibrary.wiley.com/terms-and-conditions) on Wiley Online Library for rules of use; OA articles are governed by the applicable Creative Commons License

by [40]:

$$FE = F_{ex} \times F_{em} = \frac{\gamma_{ex}}{\gamma_{ex}^{0}} \times \frac{q}{q^{0}} \quad (6)$$

where F_{ex} and F_{em} represent the excitation enhancement factor and the quantum yield enhancement factor, respectively. Specifically, γ_{ex} ($\gamma_{ex}{}^{0}$) represents the excitation rate in the presence (absence) of the nano-system during excitation, while q (q^{0}) denotes the quantum yield of the molecule in the presence (absence) of the nano-system during emission, respectively (see more simulation details in Section S6). Note that the minimum values (FE_{min}s) exist in the experimentally measured fluorescence enhancement distributions. With such experimentally determined FE_{min} thresholds incorporated, in our simulations we only need to calculate the fluorescence enhancement in certain regions on the simulation planes for two nano-systems with g = 20 nm (Figure 3d, bottom panel). Specifically, in the hybrid system we only need to incorporate the hotspot region (demarcated by the black dashed box in Figure 3g top panel), whereas in the nanoantenna-only system we need to study the fluorescence enhancement of molecules in both the non-hotspot (demarcated by the grey dashed box in Figure 3g top panel) and hotspot regions. A comparison of experimental and simulated distributions for identical systems show that they agree well with each other, with only two discrepancies observed. First, the experimentally measured distribution for the nanoantenna-only system exhibits a significantly lower FE_{max} than that of the simulated one, which is understandable since high-enhancement events of extremely low probabilities in the simulated distributions are nearly impossible to detect under low-concentration experimental conditions. Second, the simulated fluorescence enhancement distribution for the hybrid system shows a higher probability of high-enhancement events compared to the experimental distribution. This discrepancy arises because we performed FEM simulations on a simplified 2D model instead of the actual system, which can save prohibitive computational costs yet can still yield reasonably reliable results (see Section S6 for more simulation details). We note that the simulated distribution obtained from simulations across seven planes, as presented in Figure S21, shows quantitatively better agreement with experimental results. However, such kind of simulations are too time consuming, and thus we perform numerical simulations on the 2D model for all systems that we consider in this manuscript.

The agreement between experimental and simulation results demonstrates that shielding the nanoantenna's non-hotspot regions with the nanoaperture mask, while reducing the number of detectable molecules by blocking ~90% of the antenna's low-enhancement area, critically enhances the probability of molecules entering the hotspot regions. This architecture not only achieves significantly higher FE_{max} and FE_{avg} compared to bare nanoantenna arrays, but also ensures more uniform fluorescence enhancement across individual dye molecules while substantially reducing fluorescence background. As a result, the system achieves more than 13 times improvement in the average SBR over its nanoantenna-only counterpart under 10 nM dye concentration. The SMFD performance of such hybrid system can be further improved by optimizing the gap size, the geometrical symmetry of double-bar nanoantenna and the nanoaperture size, as demonstrated in the subsequent sections.

2.3 | Influences of Nanoantenna Gap Size on Fluorescence Enhancement Performance

We first investigate how the gap size (i.e. g) of the double-bar nanoantenna influences the fluorescence enhancement performance of our nano-system. We fabricate a hybrid system with g = 30 nm and its nanoantenna-only counterpart, then experimentally characterize their fluorescence enhancement performances employing the same experimental technologies as in Section 2.2. Experimental results on SMFD (Figure 3f top panel) reveal that the hybrid system with g = 30 nm exhibits FE_{max} and FE_{avg} that are 2.15 and 4.36 times higher than those of its nanoantenna-only counterpart, respectively. However, this hybrid system provides an average SBR enhancement of 10.6 times over its nanoantenna-only counterpart, which is lower than that (~13.3 times) achieved by the g = 20 nm hybrid system, although both systems exhibit largely similar molecule detection efficiency. This observed difference in SBR enhancement is further validated by high-concentration FCS experiments (see Figure S14 and Table S8): under 10 μM Alexa555 conditions, the g = 30 nm hybrid system yields an average SBR enhancement of 13.7 times over its nanoantenna-only counterpart, significantly lower than that (17.8 times) achieved by the g = 20 nm hybrid system, while both systems exhibited a comparable number of enhanced molecules in the FCS measurements. Such experimental trend is consistent with our numerical simulations. As depicted in Figure 3g, simulated fluorescence enhancement in the hotspot region is visibly weaker in the g = 30 nm system (bottom panel) compared to the g = 20 nm one (top panel). Therefore, both experimental and simulation results confirm that nanoantenna with a smaller gap size can help achieve a better fluorescence enhancement performance for the hybrid system.

We find that combining double-bar nanoantennas with a nanoaperture can help better highlight the advantage of the nanoantenna with higher field enhancement. Obviously, the nanoantenna with a smaller gap exhibits higher field enhancement, resulting in greater fluorescence enhancement [41]. However, we find that the enhancement distributions of two nanoantenna-only systems (with g = 20 nm, 30 nm) do not exhibit obvious difference. Intriguingly, after the nano-aperture layers are added to form two hybrid systems, we find from Figure 3d,f that their corresponding fluorescence enhancement distributions show clear differences. Specifically, the g = 20 nm system performs obviously better than the g = 30 nm one, in terms of both FE_{max} and FE_{avg}. Numerical simulations confirm these experimental findings and help us understand the underlying physics. Although a nanoantenna with a smaller gap size indeed exhibits higher *FE*, with extensive non-zero-*FE* areas extending outside the hot-spot region, the probability of molecule accessing the extremely-high-*FE* region is still low in the nanoantenna-only system, which does not highlight the advantage of the small-gap nanoantenna. In sharp contrast, with non-hot-spot regions completely blocked in the hybrid systems, the probability of molecule accessing the extremely-high-*FE* region is specifically enhanced by the nanoaperture, thus significantly highlighting the advantage of the small-gap nanoantenna.

21951071, 2026, 42, Downloaded from https://advanced.onlinelibrary.wiley.com/doi/10.1002/adom.72016 by Fudan University, Wiley Online Library on [15/11/2026]. See the Terms and Conditions (https://onlinelibrary.wiley.com/terms-and-conditions) on Wiley Online Library for rules of use; OA articles are governed by the applicable Creative Commons License

2.4 | Influences of Asymmetry of Nanoantenna Design on Fluorescence Enhancement Performance

To further optimize the fluorescence enhancement performances of our hybrid systems, we employ an asymmetric double-bar nano-antenna design, which supports multiple plasmonic modes as demonstrated in our previous study [40]. The asymmetry provides an additional degree of freedom to tune two resonant modes supported by the nanoantennas, whose frequencies can well align with the excitation and emission frequencies of our molecules, respectively. We select Merocyanine (MC) as the target dye molecule, which is a commonly used photochromic dye and the open-ring form of Spiropyran (see Figure S22 in Section S7) [42], serving as an optical switch widely applied in chemical detection and cellular imaging [43, 44]. MC exhibits substantial Stokes shift (~100 nm) and relatively low quantum efficiency (~10%), providing valuable rooms for asymmetric nanoantenna design and quantum yield enhancement (see Figure S23 and Table S9). In our nano-systems designed for MC, both symmetric and asymmetric nanoantennas are utilized for comparison, with their geometric parameters given in the caption of Figure 4. We fabricate nano-systems with symmetric or asymmetric nanoantennas, with and without the nanoaperture layers, respectively. We then characterize the fluorescence enhancement performances of these systems employing the same experimental methods and conditions as in Section 2.2, only with 10 nM Alexa555 replaced by 38 nM MC (see Figures S24 and S25).

Figure 4a,b present, respectively, the measured fluorescence enhancement distributions for hybrid systems with asymmetric and symmetric nanoantennas, compared with measured results on their corresponding nanoantenna-only systems. In addition to confirming the notion that hybrid systems do exhibit better fluorescence enhancement performances than their nanoantenna-only counterparts despite detecting fewer molecules (also see Figure S26 in Section S8), these experimental results uncover a new fact: the hybrid system with asymmetric nanoantennas performs better than that with the symmetric one, in terms of both FE_{max} and FE_{avg}. Notably, while both hybrid systems exhibit largely comparable molecule detection efficiency, we find that the asymmetric hybrid system yields a 16.2 times enhancement on average SBR for SMFD, which is higher than that (13.8 times) achieved with its symmetric counterpart, considering the reduction on measured fluorescence background (see Figure S7b,c). We employ the same simulation method to numerically study the fluorescence enhancement distributions of these nano-systems, and find that they (lower panels in Figure 4a,b) are generally in good agreement with corresponding experimental results (top panels in Figure 4a,b).

To reveal the underlying physics, we conduct numerical simulations to analyze how F_{ex}, F_{em}, and FE vary as a molecule is located at different positions within the gap regions of two different nanoantennas (see Figure 4c right panels for FE, with F_{ex} and F_{em} distributions available in Figure S27). We note that F_{ex} corresponds to the local field experienced by the molecule in the excitation process, which can be obtained by computing the field distribution inside the structure under external excitation. F_{em}, however, is much more complicated to obtain, as it involves not only coupling the molecule to the nanoantenna but also the radiation from the excited nanoantenna. We obtain F_{em} through calculating the power radiated from the whole system where the molecule, excited at its emission frequency, is placed at different positions. As these two physical quantities are dictated by two distinct physics processes, it is not surprising to see that F_{ex} and F_{em} exhibit distinct distributions (see Figure S27). Specifically, whereas F_{ex} only favors a stronger local field, F_{em} is a competing result of several factors: local field, energy dissipation due to nanoantenna absorption and enhanced radiation due to excited nanoantenna.

Figure 4d illustrates the position dependences of FE (black line), F_{em} (blue line) and F_{ex} (red line) along the central line across the gap, for both symmetrical and asymmetrical nanoantennas. In the symmetric case (see bottom panel of Figure 4d), both F_{em} and F_{ex} exhibit a centrally symmetrical profile dictated by the reflection symmetry processed by two systems. Meanwhile, while F_{ex} is maximized on two metallic surfaces where local fields are strongest, F_{em} is, however, minimized on those positions due to significantly enhanced metallic absorption. Such a misalignment between F_{em} and F_{ex} lowers the peak value of total FE achieved in the symmetric system, which is about 32-fold in this particular case (see black line in lower panel of Figure 4d). In contrast, through tuning the structural asymmetry of the asymmetric nanoantenna, we can significantly bias the F_{ex} distribution to one side (see blue line in top panel of Figure 4d) thus creating an overlap between regions with high F_{ex} and high F_{em}, thereby enhancing the overall FE. As shown in the upper panel of Figure 4d, the maximum FE achieved is enhanced to over 40-fold at a non-center position in the asymmetric nanoantenna. Simulated 2D fluorescence enhancement distributions for two systems (see Figure 4c) reaffirm that the asymmetric nano-antenna exhibits an asymmetric distribution with a higher peak FE, compared to its symmetric counterpart.

The distinct spatial fluorescence enhancement maps of two bare nano-antennas can help us understand the measured fluorescence enhancement distributions of two hybrid systems, based on the similar mechanisms presented in last subsection. Although the asymmetric nanoantenna does exhibit a higher FE_{max} than the symmetric one, without the nanoapertures to shield out the non-hot-spot regions, such an advantage is not clearly highlighted in our experiments (see purple and blue bars in Figure 4a,b). In the presence of nanoapertures, however, differences between measured fluorescence enhancement distributions of two hybrid systems are obviously amplified (see orange and green bars in Figure 4a,b), which highlights the advantages of the asymmetric design.

2.5 | Influences of Nanoaperture Size on Fluorescence Enhancement Performance

Finally, we investigate the influence of nanoaperture size on the fluorescence enhancement performance of our hybrid system in order to seek for the optimal design of our nanoaperture mask. To mitigate fabrication constraints, including specifically the nanoscale alignment challenges associated with smaller apertures and the risk of Ti deposition onto nanoantennas during oblique evaporation at larger aperture sizes, we fix the width (W_H)

21951071, 2026, 42, Downloaded from https://advanced.onlinelibrary.wiley.com/doi/10.1002/adom.72016 by Fudan University, Wiley Online Library on [15/11/2026]. See the Terms and Conditions (https://onlinelibrary.wiley.com/terms-and-conditions) on Wiley Online Library for rules of use; OA articles are governed by the applicable Creative Commons License

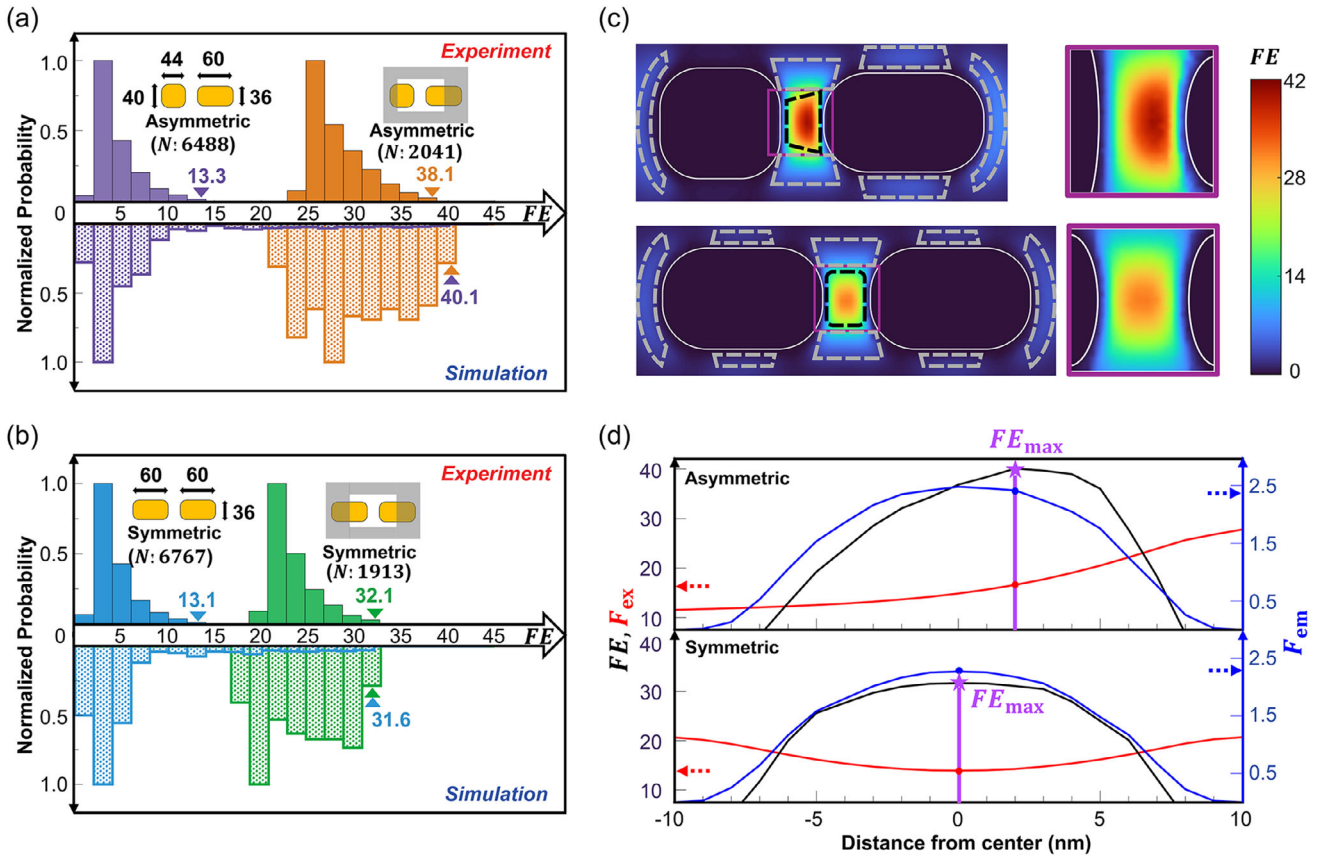

FIGURE 4 | Fluorescence enhancement of Merocyanine by nano-systems with various nanoantenna configurations. (a) Fluorescence enhancement distributions for various nano-systems with asymmetric configuration. Purple/orange: nanoantenna-only/hybrid systems. Fill/dot: experimental/simulated distributions. (b) Fluorescence enhancement distributions for various nano-systems with symmetric configuration. Blue/green: nanoantenna-only/hybrid systems. Fill/dot: experimental/simulated distributions. (c) Simulated fluorescence enhancement distributions on the plane of maximum enhancement (parallel to the substrate) for the double bar nanoantenna. Top/bottom: nanoantennas with asymmetric/symmetric configuration. Left: full structure (purple-outlined gap); right: gap magnified. Gray dashed boxes: non-hotspot regions; black dashed boxes: hotspot regions. In (a) and (b), fluorescence enhancement distributions within (hotspot + non-hotspot)/hotspot regions in (c) are assigned to the nanoantenna-only/hybrid systems' simulated distributions, N is the number of detected molecules and the FE_{max} are marked with arrows and text of the corresponding color. (d) Horizontal cut along the gap region images in (b) and Figure S27 (in Section S8) showing the FE (black), F_{ex} (red) and F_{em} (blue) along the nanoantennas' long axes for asymmetric (top) and symmetric (bottom) nanoantennas. Purple dashed lines: FE_{max} positions. Dashed red and blue arrows: F_{ex} and F_{em} value at the position of FE_{max}. Nanoantenna parameters: asymmetric $b_1 = 44$ nm, $b_2 = 60$ nm; $w_{b1} = 40$ nm, $w_{b2} = 36$ nm; $h_b = 50$ nm; $g = 20$ nm, and symmetric $b_1 = b_2 = 60$ nm; $w_{b1} = w_{b2} = 36$ nm; $h_b = 50$ nm; $g = 20$ nm. $I_x = 360$ nm; $I_y = 300$ nm. Nanoaperture parameters: $L_H = 80$ nm, $W_H = 50$ nm.

of Ti nanoaperture at 50 nm and vary the length (L_H) of nanoaperture to fabricate two series of hybrid systems, incorporating asymmetric nanoantennas designed for MC (Figure 5a) and symmetric nanoantennas designed for Alexa555 (Figure 5b), respectively. We then conduct TIRF experiments on these systems employing the same experimental technologies as in previous subsections. We find from Figure 5a,b that all hybrid systems, regardless of their L_H sizes, perform superior fluorescence enhancement than their nanoantenna-only counterparts. Furthermore, the hybrid systems with $L_H = 80$ nm always yield the best fluorescence enhancement performances among three samples with different L_H, irrespective of the nanoantenna type and the molecule used in our experiments. Additionally, the hybrid systems consistently detected fewer molecules compared to their nanoantenna-only counterparts, with the extent of reduction inversely correlated to the L_H size—smaller apertures corresponded to fewer detected molecules (see Table S3).

The observed dependence of fluorescence enhancement performances on L_H may be attributed to multiple factors. First, the alignment precision during fabrication is a critical consideration, particularly for the smallest aperture size ($L_H = 60$ nm). In single measurements (see Figure S28), we observed significant variability in fluorescence enhancement performance across different $L_H = 60$ nm samples. This variability stems from inherent limitations in our nanolithography process, where alignment accuracy can vary between the center and edge regions of the arrays. To minimize this confounding factor, we fabricated numerous $L_H = 60$ nm samples and, for detailed analysis, selected only those structures exhibiting center-region alignment offsets below 5 nm. Given that this controlled dataset still shows $L_H = 80$ nm samples yielding the optimal enhancement (Figure 5a,b), we sought to explore potential physical mechanisms beyond alignment variations. Accordingly, we developed a theoretical model to elucidate why an optimal nanoaperture size exists

21951071, 2026, 42, Downloaded from https://advanced.onlinelibrary.wiley.com/doi/10.1002/adom.72016 by Fudan University, Wiley Online Library on [15/11/2026]. See the Terms and Conditions (https://onlinelibrary.wiley.com/terms-and-conditions) on Wiley Online Library for rules of use; OA articles are governed by the applicable Creative Commons License

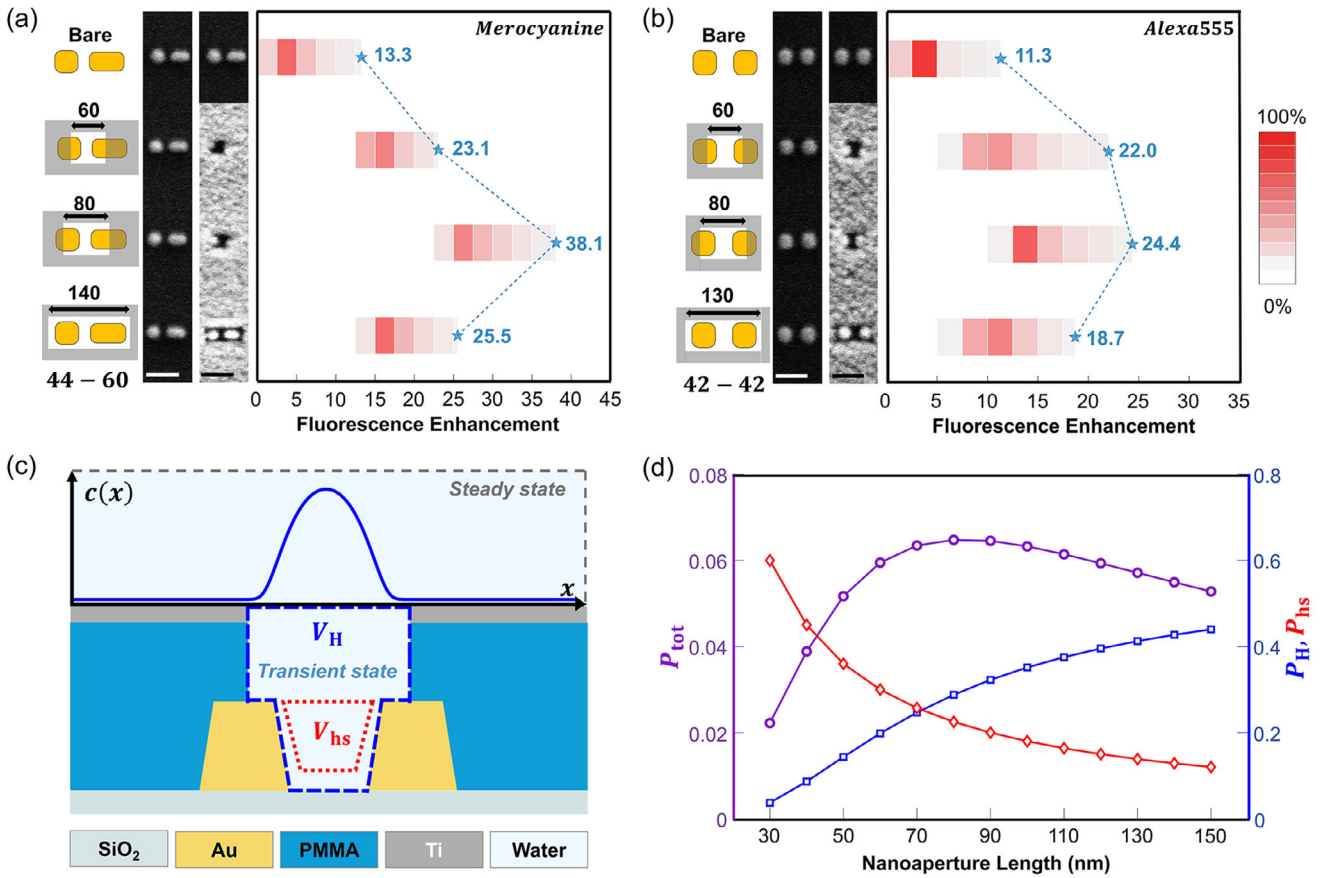

FIGURE 5 | Fluorescence enhancement of dye molecules by bare nanoantenna and nanoaperture-nanoantenna hybrid systems with different nanoaperture lengths (L_Hs). (a), (b) Experimental results for bare nanoantenna and hybrid systems with different L_Hs under two nanoantenna configurations: $b_1 = 44$ nm, $b_2 = 60$ nm; $w_{b1} = 40$ nm, $w_{b2} = 36$ nm; $h_b = 50$ nm; $g = 20$ nm (a) and $b_1 = b_2 = 42$ nm; $w_{b1} = w_{b2} = 44$ nm; $h_b = 40$ nm; $g = 30$ nm (b). Top to bottom: bare nanoantenna; $L_H = 60$ nm; $L_H = 80$ nm; $L_H = 140$ nm for (a) / 130 nm for (b). Left to right: schematic diagrams; scanning electron microscopy images; experimental fluorescence enhancement distribution. Scale bar: 100 nm. (c) Theoretical model schematic. Boltzmann distribution $c(x)$ (blue curve, calculated via Equation (7)) along the nanoaperture's long axis through its center. V_H and V_{hs} denote nanoaperture and hotspot volumes, respectively. Molecules exhibit steady-state behavior in solution above the Ti layer and transient behavior within the nanoaperture. (d) Simulated probabilities P_H (blue), P_{hs} (red) and P_{tot} (purple) versus nanoaperture size. Shared parameters for (a) and (b): $I_x = 360$ nm; $I_y = 300$ nm; $W_H = 50$ nm.

for maximizing fluorescence enhancement performance. As schematically shown in Figure 5c, we consider the distributions of molecules in different regions within the hybrid system. First of all, our TIRF observations reveal a time-invariant molecule detection rate (see Figure S29 in Section S9), indicating that molecules in the solution above the Ti layer have reached a macroscopic steady-state distribution. However, this steady-state exists only at large spatial scales and long timescales. At the microscopic level, defined by the nanoaperture volume beneath the Ti layer (nanometer spatial scale) and molecular diffusion time (microsecond timescale, see Tables S7 and S8), molecules exhibit transient Brownian motion and remain in a transient state. For molecules in the transient state, we assume that they satisfy a random spatial distribution, with equal probability of excitation at any location within the system. Meanwhile, for molecules in the steady state, they should satisfy a Boltzmann distribution (see more details in Section S9) [45]:

$$c\ (\boldsymbol{r}) = c_0\ \exp\left(\frac{Re\,[\alpha]}{2k_B T}|\boldsymbol{E}\,(\boldsymbol{r})|^2\right) \tag{7}$$

driven by both optical forces inserted by light field and the thermally induced diffusion. Here, α represents the polarizability of a fluorescent molecule, expressed by the Lorentz model as:

$$\alpha = \frac{e^2}{m}\frac{1}{\left(\omega_0^2 - \omega^2\right) - i\omega\gamma} \tag{8}$$

In fluorescence experiments, the excitation frequency ω we use is typically higher than the resonant frequency ω_0 of the dye molecules (i.e., blue detuning), resulting in $Re[\alpha] < 0$. This effect causes the molecules to accumulate in regions with weaker electric fields. Due to the edge effect, electric field is stronger near the edges of nanoapertures, leading to lower molecular probability density in those regions. Conversely, the central region, characterized by a weaker field, exhibits a higher molecular density. To quantitatively describe the role of the nanoaperture size, we use P_{tot} to denote the total probability of a molecule being excited within the system's hotspot region:

$$P_{tot} = P_H \times P_{hs} \tag{9}$$

21951071, 2026, 42, Downloaded from https://advanced.onlinelibrary.wiley.com/doi/10.1002/adom.72016 by Fudan University, Wiley Online Library on [15/11/2026]. See the Terms and Conditions (https://onlinelibrary.wiley.com/terms-and-conditions) on Wiley Online Library for rules of use; OA articles are governed by the applicable Creative Commons License

with

$$P_{\mathrm{H}} = \frac{\iint_{\boldsymbol{r}\in S} c\,(\boldsymbol{r})\,ds}{c_{\mathrm{bg}} S} \tag{10}$$

$$P_{\mathrm{hs}} = \frac{V_{\mathrm{hs}}}{V_{\mathrm{H}}} = \frac{const}{L_{\mathrm{H}}} \tag{11}$$

here, P_{H} serves as an indicator of the steady-state process, representing the probability of molecules accessing the nanoapertures, while P_{hs} acts as an indicator of the transient-state process, denoting the probability that a molecule entering the nanoaperture subsequently undergoes excitation within the hotspot region. In Equation (10), c_{bg} denotes a normalized parameter derived from the background electromagnetic field via Equation (7), $S = L_{\mathrm{H}} \times W_{\mathrm{H}}$ represents the area of the nanoaperture, and the electric fields contributing to the distribution density were simulated using the same settings as those for top-right panel of Figure 3e. In Equation (10), V_{hs} is the volume of the hotspot region, and V_{H} is the volume of the nanoaperture. We find that P_{H} and P_{hs} exhibit opposing trends as L_{H} varies (Figure 5d), indicating a possible competition between them. Specifically, as L_{H} increases, edge effect of the electric field becomes weaker, allowing more molecules to enter the nanoapertures. On the other hand, the enlarged volume of nanoaperture reduces the probability of molecules being excited within the hotspot regions. These competing effects must result in an optimal L_{H} based on which the best fluorescence enhancement performance is achieved, providing a qualitative explanation on the observed effect. Critically, the nanoaperture geometry restricts detection exclusively to molecules that enter the aperture volume, thereby reducing the detected molecule count but suppressing the background. We therefore calculate the experimental nanoaperture entry probability directly from the detected molecule counts at varying L_{H}. This enables experimental calibration of the background electromagnetic field normalization parameter c_{bg} in Equation (10), achieving quantitative agreement between theoretical P_{H} predictions and experimental values (see Figure S30). The calibrated model yields an optimal $L_{\mathrm{H}} \approx 80$ nm, consistent with our experimental results.

We note that the optimal nanoaperture size is not a fixed value, but may depend on specific experimental environments and conditions. As indicated by Equation (7), several factors, such as the molecular polarizability α (influenced by molecule properties and the solution environment), the electric field strength $|\boldsymbol{E}(\boldsymbol{r})|$ (modulated by incident light intensity), and temperature T (subject to environmental fluctuations), can affect the steady-state distribution, which in turn, change the optimal nanoaperture size (see Figure S31 in Section S10).

3 | Conclusion

In summary, we propose a novel nanoaperture-nanoantenna hybrid system and experimentally demonstrate that it can achieve up to 16 times improvement on SBR of SMFD over its nanoantenna-only counterpart. We demonstrate that this enhancement arises from nanoapertures concentrating dye molecules into the hot-spot regions while shielding the non-hot-spot regions, thereby amplifying fluorescence signals and suppressing background–albeit at a lower molecule detection proportion. We experimentally identified the roles of various geometric parameters in our hybrid systems, and found that combining a nanoantenna with a nanoaperture exhibiting an optimized size matching its hot-spot region can yield better fluorescence enhancement performance. Our studies proposed a new plasmonic architecture for ultra-sensitive SMFD featuring concentration-insensitive performance with broad operating concentrations, enhanced capture of high-fluorescence molecules despite reduced throughput, and molecular discrimination potential (see Figures S32 and S33, Table S10 in Section S11). The hybrid system enables molecules to interact exclusively with the hot-spot region of the nanoantenna. In biomolecular dynamics studies, protein or nucleic acid samples labeled with FRET pairs can be directed to bind only to the nanoantenna hot spot, achieving optimal fluorescence enhancement and substantially improving the spatiotemporal resolution of FRET. In nanophotonics, this strategy can be further extended to allow molecules to interact only with specific sites of nanostructures, making it particularly suitable for studying light–matter interactions in different regions of complex geometric nanoantennas (e.g., trimers and tetramers). These capabilities allow the platform to find many applications in chemical sensing, biomedical diagnostics, and nanoscale optical technologies.

4 | Methods

4.1 | Sample Preparation

After piranha cleaning and N_2 drying of 170 um glass substrates (Fisher-brand, No:12541015), a 200 nm/75 nm bilayer MMA/PMMA resist was spin-coated (3000 rpm, 40 s) and baked (3 min). A 10-nm Al conductivity layer was deposited via electron-beam evaporation before patterning nanoantenna arrays (45 × 45 um^2) using electron-beam lithography (JBX-8100FS). Post-exposure processing included NaOH etching (0.02 M, 90 s), development in ice-bath MIBK:IPA (1:3, 30 min), and IPA stopping (3 min). Subsequent Ti (1 nm)/Au (40 or 50 nm) metallization by electron-beam evaporation (Kurt J. Lesker, LAB-18) and acetone lift-off yielded pristine antennas, which were then oxidized in 30% H_2O_2 (10 min) to convert Ti adhesion layers to TiO_2 for enhanced optical properties. For nanoaperture integration, a PMMA/Al coating and second electron-beam lithography exposed nanoapertures at antenna sites using nanometer-scale alignment with first-stage markers. After post-exposure processing, oblique Ti deposition at 70° created aperture masks that prevented contact with antennas/substrate while exclusively exposing nanoantenna hotspots to enable solution-phase dye access.

4.2 | Scanning Electron Microscopy and Transmission Spectrum Measurement

Scanning electron microscopy images were acquired using a Zeiss Sigma 300 (2 kV, 11.2 mm WD, 100 000×). Transmission spectra were measured under aqueous conditions using a custom visible spectrum system: a supercontinuum laser (OYSL, SC-Pro) with polarization aligned to the long axis of the nanoantennas

21951071, 2026, 42, Downloaded from https://advanced.onlinelibrary.wiley.com/doi/10.1002/adom.72016 by Fudan University, Wiley Online Library on [15/11/2026]. See the Terms and Conditions (https://onlinelibrary.wiley.com/terms-and-conditions) on Wiley Online Library for rules of use; OA articles are governed by the applicable Creative Commons License

illuminated the sample, and spectra were recorded with an Ocean Insight USB4000-VIS-NIR spectrometer. For each hybrid system, its spectrum was normalized against reference spectrum from nanoantenna-free nanoaperture arrays (with the identical nanoaperture dimensions) on the same substrate. For nanoantenna-only systems, all spectra were normalized against reference spectrum of a bare glass substrate.

4.3 | Fluorescence Experimental Setup

TIRF measurements employed a home-built TIRF microscope (Olympus IX71 base, Nikon 100×/1.49 NA oil-immersion objective, motorized XY stage). Alexa555 or MC was excited with a 532 nm laser, polarized parallel to the nanoantenna's long axis, at constant power density (0.662 kW cm^{-2}). Emission was filtered (532 nm notch, 525–630 nm bandpass) and detected by an electron-multiplying charge-coupled device (EMCCD, Andor-iXon-Ultra-897, 33 ms exposure, gain = 10).

Nanoantenna-integrated samples were pre-wetted by 10 mM HEPES 0.5% Triton X-100 pH 7.5 buffer (HEPES-TX buffer) (Triton X-100 was added to enhance solution wettability and solubilize hydrophobic MC), then incubated in dye solution: Alexa555 (10 nM in HEPES-TX) or MC (20 μM Spiropyran (SP) in HEPES-TX, UV-converted). Glass references used 125 pM Alexa555 or 1 μM SP + MC. Per sample group, 90 s video recordings were acquired with eight replicates (total observation time 12 min) to establish statistical distributions, while glass-only reference groups were measured in triplicate for baseline statistics.

Confocal FCS experiments utilized a custom-built confocal microscope (Olympus IX71 base, Olympus 60×/1.40 NA oil-immersion objective) equipped with a 532 nm laser, emission filters (532 nm notch, 550–650 nm bandpass), a 50 μm pinhole, and a single-photon detector (Becker&Hickl, HPM-100-40). For single-molecule validation, identical dye solutions as TIRF experimental groups (10 nM Alexa555 or 20 μM SP + MC in HEPES-TX) were excited on bare glass coverslips at 25 μW laser power, with FCS traces acquired for 60 s each. For high-concentration fluorescence enhancement measurements, both nanoantenna-integrated samples and glass-only references were pre-wetted with HEPES-TX buffer, incubated in 10 μM Alexa555 (in HEPES-TX), then excited at 10 μW laser power and measured with 30-second acquisition per trace.

4.4 | TIRF Data Screening Method

To guarantee fluorescence signals detected by TIRF originate from single molecules, confocal FCS experiment was first performed to confirm the predominance of monomeric dye molecules in solution (diffusion time <33 ms). Building on this foundation: reference groups employed a uniform SBR threshold for fluorescent spot selection due to ultralow background, while nanoantenna-integrated experimental groups utilized a hard threshold (derived from glass reference group intensity distributions) to address high background fluorescence. All selected spots were required to exhibit single-step transitions in intensity trajectories (appearance and disappearance within adjacent frames) with maximum intensity duration ≤2 frames. High-intensity outliers with extremely low occurrence probability were concurrently excluded. This procedure maximizes the probability that the spots included in the statistics originate from single molecules. More details can be found in Section S4.

4.5 | Numerical Simulations

We employed FEM simulations using the commercial software COMSOL Multiphysics. The relative permittivity of Au was described by the Drude model $\varepsilon_{Au}(\omega) = \varepsilon_{\infty} - \frac{\omega_p^2}{\omega(\omega+i\gamma)}$, with $\varepsilon_{\infty} = 9$, $\omega_p = 2\pi \times 2175$ THz, and $\gamma = 3 \times 2\pi \times 17.71$ THz. The factor of 3 in the damping term was determined by fitting to our experimental data. The glass substrate was treated as a lossless dielectric with relative permittivity $\varepsilon_r = 1.51^2$ and the relative permittivity of water was set to $\varepsilon_{water} = 1.33^2$. More details can be found in Section S6.

Author Contributions

T.C. fabricated all samples and carried out all experiments; Z.Z. did all calculations and simulations; Q.H. and L.Z. provided technical support for simulations; B.L. provided support for part of experiments; L.Z. and Y.-W. T. conceived the idea and supervised the project. All authors contributed to the discussion and preparation of the manuscript.

Acknowledgements

This work was supported by the National Key Research and Development Program of China (Grant No. 2022YFA1407700), the National Natural Science Foundation of China (Grants Nos. 12221004, 12474306, 62192771, and 12174070), and the Natural Science Foundation of Shanghai (23dz2260100, 23xtcx00400). We acknowledge technical support from the Fudan Nanofabrication Laboratory for sample fabrication.

Funding

This work was supported by the National Key Research and Development Program of China (Grants No. 2022YFA1407700); the National Natural Science Foundation of China (Grants Nos. 12221004, 12474306, 62192771, and 12174070); the Natural Science Foundation of Shanghai (23dz2260100, 23xtcx00400).

Conflicts of Interest

The authors declare no conflicts of interest.

Data Availability Statement

All the data supporting the findings of this study are available within this Article and its Supporting Information. Any additional information can be obtained from the corresponding authors on reasonable request.

References

1. C. Joo, H. Balci, Y. Ishitsuka, C. Buranachai, and T. Ha, "Advances in Single-Molecule Fluorescence Methods for Molecular Biology," *Annual Review of Biochemistry* 77, no. 1 (2008): 51–76, https://doi.org/10.1146/annurev.biochem.77.070606.101543.

2. W. E. Moerner, "New Directions in Single-Molecule Imaging and Analysis," *Proceedings of the National Academy of Sciences* 104, no. 31 (2007): 12596–12602, https://doi.org/10.1073/pnas.0610081104.

3. S. Shashkova and M. C. Leake, "Single-Molecule Fluorescence Microscopy Review: Shedding New Light on Old Problems,"

21951071, 2026, 42, Downloaded from https://advanced.onlinelibrary.wiley.com/doi/10.1002/adom.72016 by Fudan University, Wiley Online Library on [15/11/2026]. See the Terms and Conditions (https://onlinelibrary.wiley.com/terms-and-conditions) on Wiley Online Library for rules of use; OA articles are governed by the applicable Creative Commons License

Bioscience Reports 37, no. 4 (2017): BSR20170031, https://doi.org/10.1042/BSR20170031.

4. D. Lu, G. Zhu, X. Li, et al., "Dynamic Monitoring of Oscillatory Enzyme Activity of Individual Live Bacteria via Nanoplasmonic Optical Antennas," *Nature Photonics* 17, no. 10 (2023): 904–911, https://doi.org/10.1038/s41566-023-01265-2.

5. Y. Wang, Y. Z. Peng, Y. De Wilde, and D. Lei, "Symmetry-Breaking-Induced Off-Resonance Second-Harmonic Generation Enhancement in Asymmetric Plasmonic Nanoparticle Dimers," *Nanophotonics* 13, no. 18 (2024): 3337–3346, https://doi.org/10.1515/nanoph-2024-0118.

6. L. Xin, X. Duan, and N. Liu, "Dimerization and Oligomerization of DNA-Assembled Building Blocks for Controlled Multi-Motion in High-Order Architectures," *Nature Communications* 12, no. 1 (2021): 3207, https://doi.org/10.1038/s41467-021-23532-y.

7. J. H. Kim, J. Y. Lee, E. S. Kim, and M. Y. Jeong, "Electric Field Enhancement of Coupled Plasmonic Nanostructures for Optical Amplification," *PhotoniX* 4, no. 1 (2023): 8, https://doi.org/10.1186/s43074-023-00086-4.

8. Z. Lu, J. Ji, H. Ye, H. Zhang, S. Zhang, and H. Xu, "Quantifying the Ultimate Limit of Plasmonic Near-Field Enhancement," *Nature Communications* 15, no. 1 (2024): 8803, https://doi.org/10.1038/s41467-024-53210-8.

9. R. Chikkaraddy, A. Xomalis, L. A. Jakob, and J. J. Baumberg, "Mid-Infrared-Perturbed Molecular Vibrational Signatures in Plasmonic Nanocavities," *Light: Science & Applications* 11, no. 1 (2022): 19, https://doi.org/10.1038/s41377-022-00709-8.

10. R. M. Córdova-Castro, B. van Dam, A. Lauri, et al., "Single-Emitter Super-Resolved Imaging of Radiative Decay Rate Enhancement in Dielectric Gap Nanoantennas," *Light: Science & Applications* 13, no. 1 (2024): 7, https://doi.org/10.1038/s41377-023-01349-2.

11. P. Zhan, M. J. Urban, S. Both, et al., "DNA-Assembled Nanoarchitectures With Multiple Components in Regulated and Coordinated Motion," *Science Advances* 5, no. 11 (2019): aax6023, https://doi.org/10.1126/sciadv.aax6023.

12. X. Lu, G. Ye, D. Punj, R. C. Chiechi, and M. Orrit, "Quantum Yield Limits for the Detection of Single-Molecule Fluorescence Enhancement by a Gold Nanorod," *ACS Photonics* 7, no. 9 (2020): 2498–2505, https://doi.org/10.1021/acsphotonics.0c00803.

13. S. Bidault, A. Devilez, V. Maillard, et al., "Picosecond Lifetimes With High Quantum Yields From Single-Photon-Emitting Colloidal Nanostructures at Room Temperature," *ACS Nano* 10, no. 4 (2016): 4806–4815, https://doi.org/10.1021/acsnano.6b01729.

14. Q. Jiang, P. Roy, J. B. Claude, and J. Wenger, "Single Photon Source From a Nanoantenna-Trapped Single Quantum Dot," *Nano Letters* 21, no. 16 (2021): 7030–7036, https://doi.org/10.1021/acs.nanolett.1c02449.

15. P. Roy, S. Zhu, J. B. Claude, J. Liu, and J. Wenger, "Ultraviolet Resonant Nanogap Antennas With Rhodium Nanocube Dimers for Enhancing Protein Intrinsic Autofluorescence," *ACS Nano* 17, no. 22 (2023): 22418–22429, https://doi.org/10.1021/acsnano.3c05008.

16. E. K. Herkert, L. Lau, R. P. Lanau, and M. F. Garcia-Parajo, "Hexagonal Plasmonic Arrays for High-Throughput Multicolor Single-Molecule Studies," *ACS Applied Materials & Interfaces* 16, no. 31 (2024): 41271–41280, https://doi.org/10.1021/acsami.4c04744.

17. J. Liang, L. Zhang, S. Wang, Y. Yu, and D. Lei, "Temperature-Modulated VO2/Au Composite Nanoparticles for High-Performance SERS-Based Trace Detection," *ACS Applied Nano Materials* 8, no. 14 (2025): 7112–7123, https://doi.org/10.1021/acsanm.5c00380.

18. H. Xin, B. Namgung, and L. P. Lee, "Nanoplasmonic Optical Antennas for Life Sciences and Medicine," *Nature Reviews Materials* 3, no. 8 (2018): 228–243, https://doi.org/10.1038/s41578-018-0033-8.

19. S. Gao, R. Zhou, S. Samanta, J. Qu, and T. Y. Ohulchanskyy, "Recent Advances in Plasmon-Enhanced Luminescence for Biosensing and Bioimaging," *Analytica Chimica Acta* 1254 (2023): 341086, https://doi.org/10.1016/j.aca.2023.341086.

20. A. Kinkhabwala, Z. Yu, S. Fan, Y. Avlasevich, K. Müllen, and W. E. Moerner, "Large Single-Molecule Fluorescence Enhancements Produced by a Bowtie Nanoantenna," *Nature Photonics* 3, no. 11 (2009): 654–657, https://doi.org/10.1038/nphoton.2009.187.

21. D. Punj, J. de Torres, H. Rigneault, and J. Wenger, "Gold Nanoparticles for Enhanced Single Molecule Fluorescence Analysis at Micromolar Concentration," *Optics Express* 21, no. 22 (2013): 27338–27343, https://doi.org/10.1364/OE.21.027338.

22. M. J. Levene, J. Korlach, S. W. Turner, M. Foquet, H. G. Craighead, and W. W. Webb, "Zero-Mode Waveguides for Single-Molecule Analysis at High Concentrations," *Science* 299, no. 5607 (2003): 682–686, https://doi.org/10.1126/science.1079700.

23. J. Larkin, R. Y. Henley, V. Jadhav, J. Korlach, and M. Wanunu, "Length-Independent DNA Packing Into Nanopore Zero-Mode Waveguides for Low-Input DNA Sequencing," *Nature Nanotechnology* 12, no. 12 (2017): 1169–1175, https://doi.org/10.1038/nnano.2017.176.

24. W. Li, J. Zhou, N. Maccaferri, R. Krahne, K. Wang, and D. Garoli, "Enhanced Optical Spectroscopy for Multiplexed DNA and Protein-Sequencing With Plasmonic Nanopores: Challenges and Prospects," *Analytical Chemistry* 94, no. 2 (2022): 503–514, https://doi.org/10.1021/acs.analchem.1c04459.

25. M. F. Nüesch, M. T. Ivanovic, J.-B. Claude, et al., "Single-Molecule Detection of Ultrafast Biomolecular Dynamics With Nanophotonics," *Journal of the American Chemical Society* 144, no. 1 (2022): 52–56, https://doi.org/10.1021/jacs.1c09387.

26. N. Klughammer and C. Dekker, "Corrigendum: Palladium Zero-Mode Waveguides for Optical Single-Molecule Detection With Nanopores (2021 Nanotechnology32 18LT01)," *Nanotechnology* 32, no. 44 (2021): 449501, https://doi.org/10.1088/1361-6528/ac197e.

27. D. Conteduca, G. Brunetti, I. Barth, S. D. Quinn, C. Ciminelli, and T. F. Krauss, "Multiplexed Near-Field Optical Trapping Exploiting Anapole States," *ACS Nano* 17, no. 17 (2023): 16695–16702, https://doi.org/10.1021/acsnano.3c03100.

28. W. Yang, M. van Dijk, C. Primavera, and C. Dekker, "FIB-Milled Plasmonic Nanoapertures Allow for Long Trapping Times of Individual Proteins," *iScience* 24 (2021): 103237, https://doi.org/10.1016/j.isci.2021.103237.

29. D. V. Verschueren, S. Pud, X. Shi, L. De Angelis, L. Kuipers, and C. Dekker, "Label-Free Optical Detection of DNA Translocations Through Plasmonic Nanopores," *ACS Nano* 13, no. 1 (2019): 61–70, https://doi.org/10.1021/acsnano.8b06758.

30. F. Wang, C. Zhao, P. Zhao, F. Chen, D. Qiao, and J. Feng, "MoS2 Nanopore Identifies Single Amino Acids With Sub-1 Dalton Resolution," *Nature Communications* 14, no. 1 (2023): 2895, https://doi.org/10.1038/s41467-023-38627-x.

31. S. Tiwari, P. Roy, J. B. Claude, and J. Wenger, "Achieving High Temporal Resolution in Single-Molecule Fluorescence Techniques Using Plasmonic Nanoantennas," *Advanced Optical Materials* 11, no. 13 (2023): 2300168, https://doi.org/10.1002/adom.202300168.

32. A. Barulin, J. B. Claude, S. Patra, N. Bonod, and J. Wenger, "Deep Ultraviolet Plasmonic Enhancement of Single Protein Autofluorescence in Zero-Mode Waveguides," *Nano Letters* 19, no. 10 (2019): 7434–7442, https://doi.org/10.1021/acs.nanolett.9b03137.

33. A. Al Masud, W. E. Martin, F. H. Moonschi, et al., "Mixed Metal Zero-Mode Guides (ZMWs) for Tunable Fluorescence Enhancement," *Nanoscale Advances* 2 (2020): 1894–1903, https://doi.org/10.1039/C9NA00641A.

34. S. Patra, J. B. Claude, and J. Wenger, "Fluorescence Brightness, Photostability, and Energy Transfer Enhancement of Immobilized Single Molecules in Zero-Mode Waveguide Nanoapertures," *ACS Photonics* 9, no. 6 (2022): 2109–2118, https://doi.org/10.1021/acsphotonics.2c00349.

35. D. Punj, M. Mivelle, S. B. Moparthi, et al., "A Plasmonic 'Antenna-in-Box' Platform for Enhanced Single-Molecule Analysis at Micromolar

21951071, 2026, 42, Downloaded from https://advanced.onlinelibrary.wiley.com/doi/10.1002/adom.72016 by Fudan University, Wiley Online Library on [15/11/2026]. See the Terms and Conditions (https://onlinelibrary.wiley.com/terms-and-conditions) on Wiley Online Library for rules of use; OA articles are governed by the applicable Creative Commons License

Concentrations," *Nature Nanotechnology* 8, no. 7 (2013): 512–516, https://doi.org/10.1038/nnano.2013.98.

36. P. M. Winkler, F. Campelo, M. I. Giannotti, and M. F. Garcia-Parajo, "Impact of Glycans on Lipid Membrane Dynamics at the Nanoscale Unveiled by Planar Plasmonic Nanogap Antennas and Atomic Force Spectroscopy," *The Journal of Physical Chemistry Letters* 12, no. 4 (2021): 1175–1181, https://doi.org/10.1021/acs.jpclett.0c03439.

37. E. K. Herkert, D. R. Bermeo Alvaro, M. Recchia, W. Langbein, P. Borri, and M. F. Garcia-Parajo, "Hybrid Plasmonic Nanostructures for Enhanced Single-Molecule Detection Sensitivity," *ACS Nano* 17, no. 9 (2023): 8453–8464, https://doi.org/10.1021/acsnano.3c00576.

38. Y. Lin, J. Hu, W. Zhang, et al., "Broadband Single-Molecule Fluorescence Enhancement Based on Self-Assembled Ag@Au Dimer Plasmonic Nanoantennas," *Nanoscale* 14, no. 47 (2022): 17550–17560, https://doi.org/10.1039/D2NR03466B.

39. P. Ghenuche, M. Mivelle, J. de Torres, et al., "Matching Nanoantenna Field Confinement to FRET Distances Enhances Förster Energy Transfer Rates," *Nano Letters* 15, no. 9 (2015): 6193–6201, https://doi.org/10.1021/acs.nanolett.5b02535.

40. W. Zhao, X. Tian, Z. Fang, et al., "Engineering Single-Molecule Fluorescence With Asymmetric Nano-Antennas," *Light: Science & Applications* 10, no. 1 (2021): 79, https://doi.org/10.1038/s41377-021-00522-9.

41. B. Song, Z. Jiang, Z. Liu, et al., "Probing the Mechanisms of Strong Fluorescence Enhancement in Plasmonic Nanogaps With Sub-Nanometer Precision," *ACS Nano* 14, no. 11 (2020): 14769–14778, https://doi.org/10.1021/acsnano.0c01973.

42. G. Berkovic, V. Krongauz, and V. Weiss, "Spiropyrans and Spirooxazines for Memories and Switches," *Chemical Reviews* 100, no. 5 (2000): 1741–1754, https://doi.org/10.1021/cr9800715.

43. S. H. Mostafavi, F. Tong, T. W. Dugger, D. Kisailus, and C. J. Bardeen, "Noncovalent Photochromic Polymer Adhesion," *Macromolecules* 51, no. 6 (2018): 2388–2394, https://doi.org/10.1021/acs.macromol.8b00036.

44. Y. Zhan, A. P. H. J. Schenning, D. J. Broer, G. Zhou, and D. Liu, "Light-Driven Electrohydrodynamic Instabilities in Liquid Crystals," *Advanced Functional Materials* 28, no. 21 (2018): 1707436, https://doi.org/10.1002/adfm.201707436.

45. H. Risken, "Fokker-Planck Equation," in *The Fokker-Planck Equation: Methods of Solution and Applications*, ed. H. Haken (Springer, 1996).

Supporting Information

Additional supporting information can be found online in the Supporting Information section.

Supporting File: adom72016-sup-0001-SuppMat.docx.

21951071, 2026, 42, Downloaded from https://advanced.onlinelibrary.wiley.com/doi/10.1002/adom.72016 by Fudan University, Wiley Online Library on [15/11/2026]. See the Terms and Conditions (https://onlinelibrary.wiley.com/terms-and-conditions) on Wiley Online Library for rules of use; OA articles are governed by the applicable Creative Commons License